Microwave-assisted synthesis and critical analysis for YBa$_2$Cu$_3$O$_{6+\delta}$ nanoparticles

Ashish Chhaganlal Gandhi ● and Jauyn Grace Lin

Center for Condensed Matter Science, National Taiwan University, Taipei 10617, Taiwan

E-mail: jglin@ntu.edu.tw

CrossMark

Abstract

A new cost effective scheme of a microwave-assisted sol–gel route followed by a short annealing time is proposed to synthesize YBCO nanoparticles (NPs) of various sizes. The advanced techniques of synchrotron radiation x-ray diffraction (SRXRD) and electron spin resonance (ESR) are used to analyze the size effects on their magnetic/superconducting properties. The major interesting finding is that the size of YBCO NPs could confine the amount of oxygen content and consequently change the superconducting transition temperature (T_C) of YBCO NPs. The ESR result demonstrates a sensitive probe to characterize surface defects in the oxygen-deficient YBCO NPs.

Keywords: YBCO, superconductivity, oxygen occupancy, microwave synthesis, ESR

(Some figures may appear in colour only in the online journal)

1. Introduction

The world's first high-temperature superconductor YBa$_2$Cu$_3$O$_{6+\delta}$ (YBCO-δ) with a superconducting transition temperature (T_C) of 93 K, which is above the boiling point of liquid nitrogen (73 K), was discovered in 1987 [1]. The discovery of YBCO made the applications of the superconductor costless and operationally effective. However, the superconducting and electrical properties of YBCO critically depend on the excess oxygen content (δ), which requires a considerable effort to detect and control. The excess oxygen induces a structural transformation from tetragonal ($0 \leqslant \delta \leqslant 0.35$) to orthorhombic ($\delta > 0.35$) with a charge redistribution along the c-axis [2], leading to the generation of hole carriers in the a–b plane and the occurrence of superconductivity. Numerous studies have been carried out to understand the effects of δ on the physical properties of bulk YBCO, but only a few for YBCO nanoparticles (NPs) [3–13]. It is known that the physical properties of YBCO NPs depend on the particles size and surface defects associated with the synthesis methods [14]. However, the correlation between size, δ, and superconducting properties of NPs is rarely studied because of the lack of proper tools. The electron spin resonance (ESR) spectrometer is one of the sensitive probes to study the oxygen concentration by detecting the free electron of the Cu^{2+} ions of the YBCO system [15]. Fully

oxygenated YBCO bulk is ESR-silent due to the non-magnetic ground state or excessive line broadening [16, 17]. On the contrary, the mechanically grounded powders of YBCO are ESR-active, which is attributed to either the interaction between Cu ions in the chain (Cu(2)O$_5$ clusters) and those in the plane (Cu(1)O$_5$ cluster) [17], or a parasitic phase (e.g. Y$_2$BaCuO$_5$ and BaCuO$_{2+x}$) [15].

In the past, various wet chemical methods such as the soft chemical approach [13], citrate-gel [8], and citrate pyrolysis [9, 10, 12] were often used for the synthesis of YBCO NPs. Alternatively, a physical method such as microwave heating could be effective, but is less discussed [18]. The principle of microwave heating is to vibrate the electric dipoles of molecules with an electric field, resulting in a uniform heat transfer in the materials. Therefore, within a short period of time, the CuO molecule could be heated up to 550 °C by absorbing microwave radiation of 2.45 GHz to provide the energy required to form the phase of YBCO [19–22]. In this work, we propose a microwave-assisted sol–gel synthesis, followed by a short annealing time in an ambient atmosphere, to prepare size-controllable YBCO NPs. This new experimental route reduces the synthesis steps as well as the synthesis time. For a critical analysis, we use advanced probes, synchrotron radiation x-ray diffraction (SRXRD) and ESR, to obtain detailed structural and oxygen properties. Our result displays an unusual size dependency of
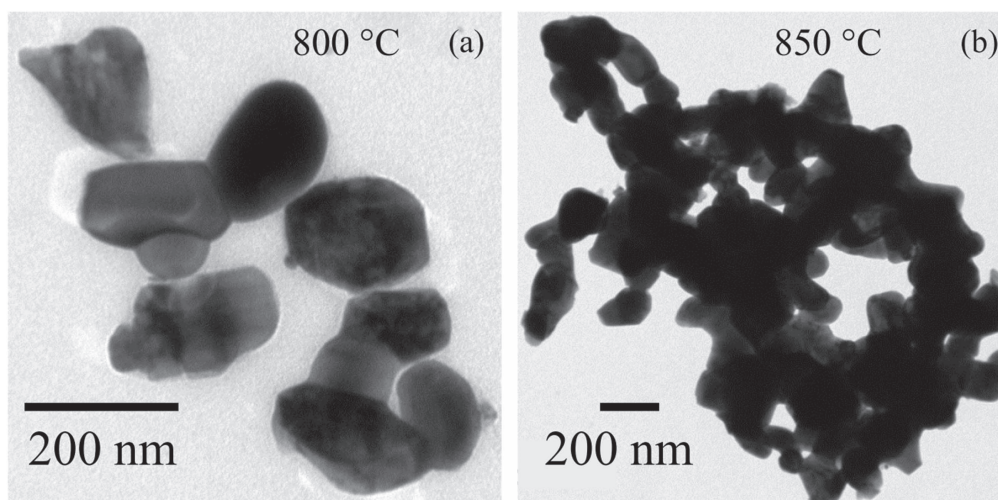
Figure 1. (a) and (b) show the TEM images of 800 °C and 850 °C annealed samples, respectively.

T_C and the lattice parameter, which is correlated with a combined effect of hole doping and size confinement.

2. Material synthesis and experimental methods

2.1. Chemicals

Yttrium nitrate hexahydrate ($Y(NO_3)_3 \cdot 6H_2O$) (99.9%, Alfa Asear), barium nitrate ($Ba(NO_3)_2$) (99.95%, Alfa Asear), copper nitrate trihydrate ($Cu(NO_3)_2 \cdot 3H_2O$) (99%, Across), citric acid ($C_6H_8O_7$) (99.5 + %, Alfa Asear), and 25% NH_4OH (Sigma Aldrich) are used. Deionized water (DIW) is used as a solvent.

2.2. Synthesis of $Y_1Ba_2Cu_3O_{6+\delta}$ NPs

A typical sol–gel method for the synthesis of $Y_1Ba_2Cu_3O_{7-\delta}$ NPs is as follows: 1.915 g of $Y(NO_3)_3 \cdot 6H_2O$, 2.613 g of $Ba(NO_3)_2$, and 3.624 g of $Cu(NO_3)_2 \cdot 3H_2O$ are dissolved in 400 ml DIW, and 6.724 g of citric acid in 200 ml DIW water, separately. To form a uniform solution, continuous magnetic stirring is employed at room temperature for 30 min. Then, the citric acid solution is added dropwise at a rate of 2 ml min^{-1} to the nitrate solution under continuous magnetic stirring. A pH equal to 3 is set at room temperature by using 25% NH_4OH. Then, the solution is exposed to a 2.45 GHz frequency at 60% power of 800 W by using a domestic microwave oven (SHART R-T20Z) for 25 min, which results in the formation of a greenish-black colored powder. The above-formed powders are then dissolved in DIW, sonicated, and re-exposed to microwave using the same microwave condition for another 25 min, which results in the formation of black colored powders. Powders are ground and used as a precursor for the preparation of different sized NPs. The post annealing temperature T_A is set as 750 °C, 800 °C, 850 °C, 920 °C, 950 °C, and 980 °C, with a duration of 2 h in air. The annealing of the precursor is carried out in a quartz tube furnace (Lindberg/Blue M, Model: TF55035A) with a heating and cooling rate of 5 °C min^{-1}.

2.3. Characterization techniques

Morphological analysis of the samples was carried out by using transmission electron microscopy (TEM) (Hitachi H-7100 operating at 200 kV). SRXRD measurements were performed at the National Synchrotron Radiation Research Center (Hyogo, Japan), Spring-8 contract beamline BL12B2, using a Rayonix MS225 (CCD) detector. The incident wavelength is 0.688 98 Å (18 keV), and the sample-to-detector distance is 149.4 mm. The measurements of temperature-dependent zero-field-cooled (ZFC) and field-cooled (FC) magnetization were carried out by using a quantum designed MPMS VSM SQUID magnetometer. The room temperature ESR spectra were taken using an X-band Bruker EMX system, and were recorded by placing powders into a quartz tube and then inserting it into a T_{102} rectangular cavity. During ESR measurements, the frequency was kept constant at 9.44 GHz, while the magnetic field H was varied from 100 to 7000 Oe with a step of 5 Oe.

3. Experimental results

3.1. Morphology and structural analysis

Figures 1(a) and (b) show the typical TEM images for 800 °C and 850 °C annealed samples, respectively. The particles of the 800 °C sample are well separated, with the size varying from ∼50 nm to 200 nm. Annealing at 850 °C results in the segregation of NPs. Annealing at and above 920 °C leads to a partial melting of YBCO, and a broad size distribution with non-uniform morphologies; this is consistent with the findings of previous reports [23–25]. Figure 2(a) shows the SRXRD spectra for 800 °C, 850 °C, 920 °C, 950 °C, and 980 °C annealed samples (bottom to top; spectra are shifted vertically for clarity). According to the data (symbols) and the fits with Rietveld refinement (solid lines), the structures of YBCO with $T_A > 800$ °C are all orthorhombic with the space group of Pmmm; meanwhile, the structure of the 750 °C sample is tetragonal (not shown here). The minor impurity phases such

Table 1. Summary of the SRXRD fitting parameters (δ = occupancy at the O(1) site, lattice constants, wRp, Rp, and χ^2) for YBCO NPs along with the reported values of orthorhombic (*) and tetragonal (#) YBCO bulks for comparison [2].

$\langle d \rangle$ (nm)	δ	a	b	c	wRp	Rp	X^2
30	0	3.8766(9)	= a	11.5926(29)	0.1787	0.1174	193.8
34	0.35	3.8567(4)	3.8820(4)	11.6344(15)	0.0611	0.0352	0.6981
39	0.75	3.8246(4)	3.8780(5)	11.6482(18)	0.0680	0.0433	1.089
42	0.71(5)	3.8172(1)	3.8798(2)	11.6711(6)	0.0391	0.0257	0.1940
44	0.73(6)	3.8163(1)	3.8809(1)	11.6812(5)	0.0204	0.0146	0.0179
45	0.64(4)	3.8161(1)	3.8813(1)	11.6809(5)	0.0235	0.0165	0.0277
*Bulk	0.73	3.8275(1)	3.8875(1)	11.7063(2)	—	—	—
#Bulk	0.09	3.8600(1)	= a	11.8162(2)	—	—	—
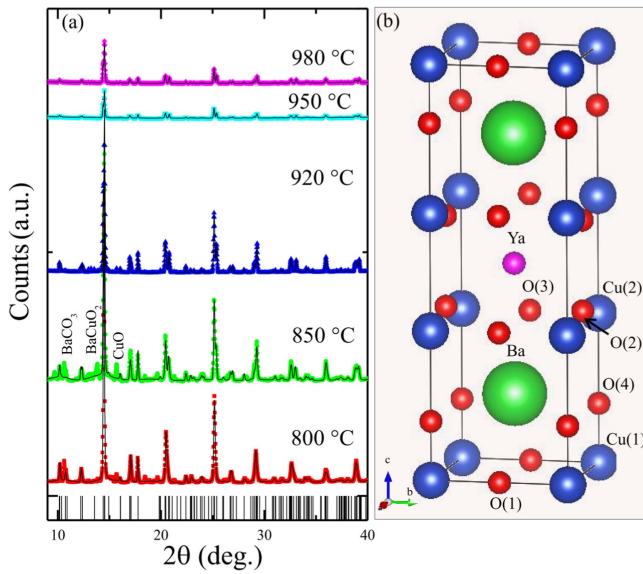
Figure 2. (a) Room temperature SRXRD spectra for the annealed samples with T_A = 800 °C to 980 °C. SRXRD spectra are shifted vertically for clear visibility. (b) A unit cell of orthorhombic YBCO.

as BaCO$_3$ (orthorhombic, Pmcn) [26] is present for T_A = 800 °C and 850 °C; BaCuO$_2$ (cubic, Im-3m) [27] and CuO (monoclinic, C2/c) [28] are present for T_A = 800 °C–920 °C. The most intensive peak located at $2\theta \sim 15.54°$ is fitted with a Lorentzian function, and its full-width-at-half-maximum (FWHM) is determined [29]. The FWHM values decrease from $0.111 \pm 0.002°$ to $0.084 \pm 0.002°$ as T_A increases from 750 °C to 980 °C. The size of the YBCO NP is calculated using Scherrer's formula: $\langle d \rangle = k\lambda / \beta \cos\theta$, where θ is the diffraction angle, β is the FWHM, λ an incident wavelength (= 0.068 898 nm), and k is the Scherrer constant (= 0.94). The $\langle d \rangle$ value for T_A = 750 °C, 800 °C, 850 °C, 920 °C, 950 °C, and 980 °C is 30, 34, 39, 42, 44, and 45 nm respectively. The increase of $\langle d \rangle$ with increasing annealing temperature is consistent with what was observed in the YBCO NPs synthesized by citrate pyrolysis [10].

The structural parameters, including oxygen site occupancy, are determined by using the Rietveld refinement for SRXRD patterns with GSAS software package [30, 31]. The sites of Y, Ba, Cu(1), Cu(2), O(2), O(3), and O(4) in a YBCO unit cell are demonstrated in figure 2(b) for a phase of full

oxygen stoichiometry ($\delta = 1$). To obtain the amount of oxygen content using the refinement method, the occupancies are constrained at their ideal values except for the oxygen occupancy at the O(1) site, the atomic positions (x, y, z) of all elements, and the lattice parameters (a, b, c). The structural parameters for YBCO NPs are summarized with a comparison of previous data in table 1, including δ (the occupancy at the O(1) site), lattice constants, wRp, Rp, and χ^2.

3.2. Superconducting properties

In order to determine T_C of NPs, the temperature-dependent magnetization M(T) is measured from 2 K to 100 K at 10 Oe, with both ZFC and FC modes. Figures 3(a)–(c) are the M(T) curves for selected samples 34, 39, and 42 nm in size. The value of T_C is defined as the onset of the superconducting transition, as indicated with arrows. Compared to bulk YBCO, a relatively broad transition is observed in all NPs due to the surface defects [32]. In figure 3(a), the ZFC curves of the 34 nm sample show a negative M from 100 K to ~20 K, which is attributed to the diamagnetic signal of BaCO$_3$ [33]. In particular, the ZFC (FC) curve shows a sharp drop (rise) at ~14 K, and a rise (drop) at ~10 K. The first transition temperature at 14(2) K is assigned to the T_C of YBCO, and is close to the reported value for YBCO-0.35 [2]. With increasing the size from 34 to 42 nm, T_C shifts drastically from 14(2) to 90(2) K. The observed transition at ~10 K is assigned to the Neel transition temperature (T_N) of the antiferromagnetic BaCuO$_2$ impurity phase [34], which manifests as the bump in the FC–M(T) curves of the 39 nm sample. The strength of magnetic shielding of the superconductor is quantified by the negative value of magnetization at 2.4 K, which increases with increasing size, and reaches a maximum value of 0.45 emu g^{-1} at 42 nm. The M(H) curves at T = 300 K with H = ± 10 kOe are shown in the inset of figure 3(b) for 34, 39, and 42 nm NPs. A weak hysteresis loop is observed for all three samples, which is assigned to the intrinsic defects such as oxygen vacancies residing on the surface of NPs [7–10, 12].

3.3. ESR analysis

ESR is a powerful tool for investigating unpaired electrons in transition metal oxides [26]. In principle, a paramagnetic
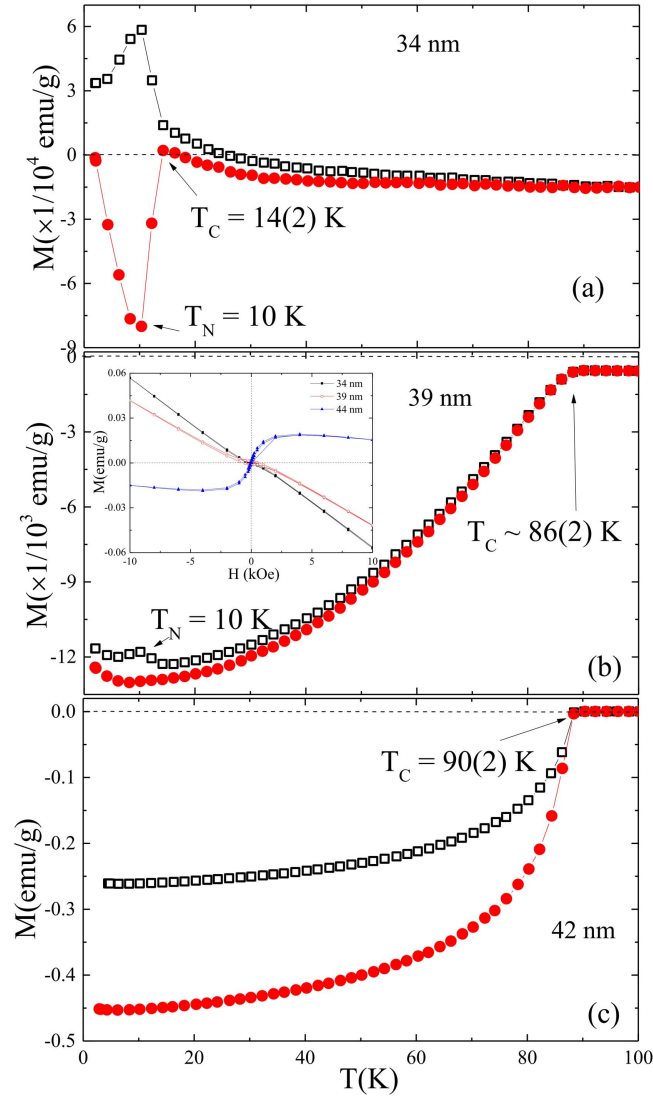
Figure 3. (a)–(c) Temperature dependent magnetization M(T) measured using the ZFC–FC process with a 10 Oe field for 34, 39, and 42 nm NPs. The inset of (b) shows the M(H) loop measured at 300 K for 34, 39, and 42 nm NPs.

sample is placed in a uniform magnetic field that splits the energy levels of the ground state by ΔE. $\Delta E = g\beta H_r = h\nu$, where ν is the microwave frequency, h is the Planks constant, β is the Bohr magnetron, H_r is the resonance field, and g is the gyromagnetic ratio of the free electron and is equal to 2.002. The spins of unpaired electrons rotate (so called precession) with the same frequency as the applied microwave when a resonance condition occurs. The value of H_r is used to calculate the g-factor, and the line-width (ΔH) represents the relaxation rate of spins. The amplitude (A) of the ESR spectrum is proportional to the concentration of unpaired electrons. The room temperature first-derivative ESR spectra as a function of H for 34, 39, and 42 nm samples are shown in figure 4 (top to bottom). Three characteristic features are observed: (i) the intensity of ESR spectra increases with the increase of particle size, and is ascribed to an increase in the concentration of paramagnetic complexes; (ii) the ESR peak at the low absorption field disappears in the 42 nm sample;
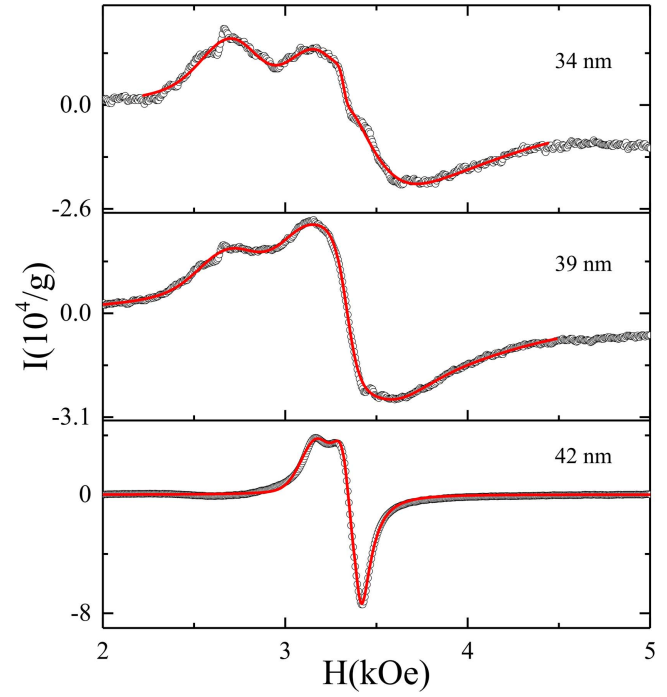

Figure 4. Room temperature first-derivative ESR absorption spectra of 34, 39, and 42 nm NPs (from top to bottom), where the solid line is the best fit obtained by deconvoluting the ESR spectrum using a sum of Gaussian and Lorentzian functions.

and (iii) the peak splitting near the free spin resonance field (Hr $\sim$ 3374 Oe) becomes more pronounced in the 42 nm sample.

Figure 5(a) is the ESR spectrum for the 39 nm NP. The spectrum is deconvoluted using a sum of two Gaussian and two Lorentzian differential functions (represented by dashed and dotted lines, respectively). The deconvolution expression can be written as follows:

$$I = I_o - \frac{4}{\sqrt{\pi/2}}\left[\frac{A_1(H - H_{r1})}{\Delta H_1^3}e^{-2\frac{(H-H_{r1})^2}{\Delta H_1^2}}\right.$$
$$\left. + \frac{A_2(H - H_{r2})}{\Delta H_2^3}e^{-2\frac{(H-H_{r2})^2}{\Delta H_2^2}}\right]$$
$$- \frac{16}{\pi}\left[\frac{A_3\Delta H_3(H - H_{r3})}{(4(H - H_{r3})^2 + \Delta H_3^2)^2}\right.$$
$$\left. + \frac{A_4\Delta H_4(H - H_{r4})}{(4(H - H_{r4})^2 + \Delta H_4^2)^2}\right],$$

where (A_1, A_2), (H_{r1}, H_{r2}), and $(\Delta H_1, \Delta H_2)$ are the amplitude, resonance field, and line-width of the two Gaussian resonance peaks, and (A_3, A_4), (H_{r3}, H_{r4}), and $(\Delta H_3, \Delta H4)$ are those of the two Lorentzian resonance peaks, respectively. Note that the best fit for 42 nm particles is obtained by using a sum of only one Gaussian and two Lorentzian differential functions. Figure 5(b) depicts the values of effective g-factors (g_i) calculated by $h\nu = \beta g_i H_{ri}$ (where $\nu = 9.44$ GHz, and $i = 1, 2, 3, 4$) with respect to particle size. The values of g_1, g_2, and g_3 decrease slightly with an increase of particle size from 34 to 39 nm, above which they show a similar value, whereas g_4
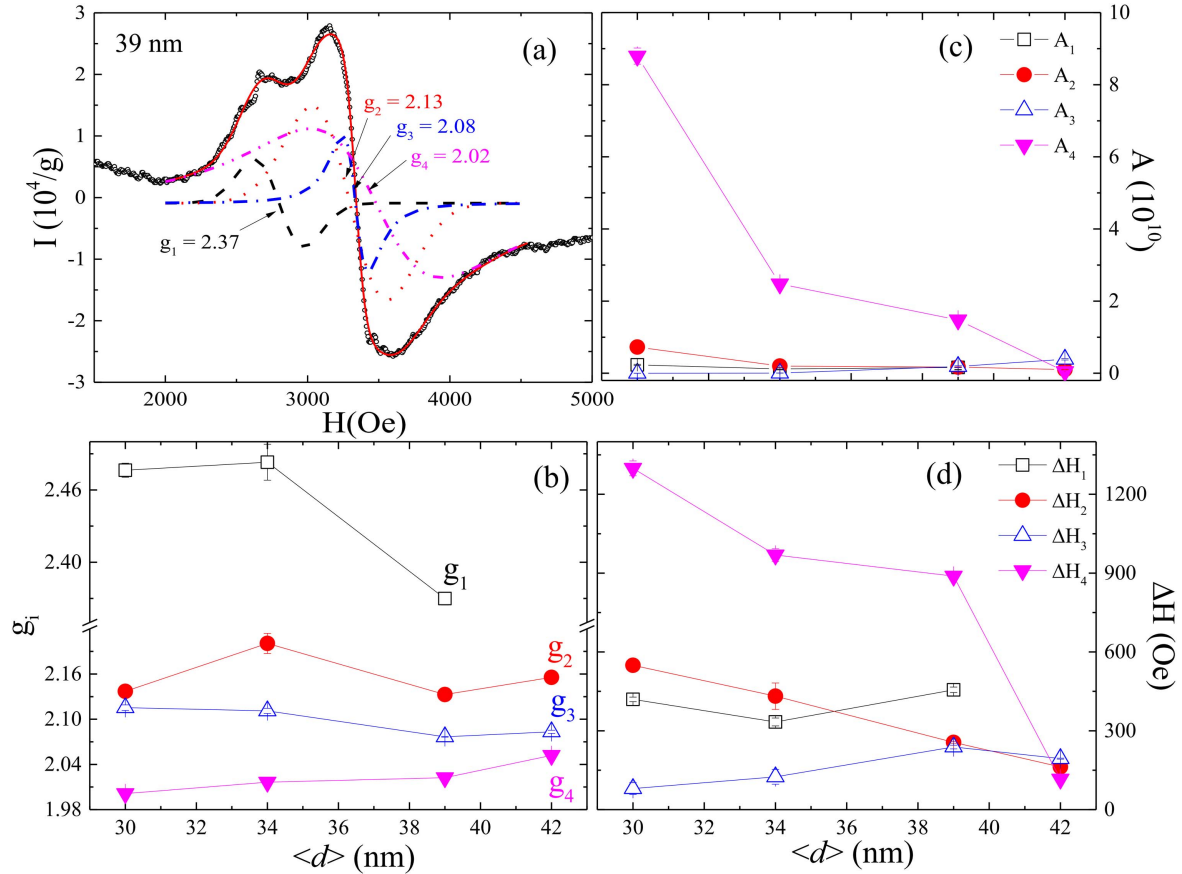
Figure 5. (a) Deconvoluted ESR spectra of 39 nm NPs using a sum of two Gaussian and two Lorentzian functions. Plot of size dependency of (b) effective g-factor, (c) amplitude, and (d) line-width of 34, 39, and 42 nm NPs.

shows a slight increment. The values of g_i for different samples remain within a range: $g_1 = 2.48 \sim 2.37$ (open squares), $g_3 = 2.12 \sim 2.08$ (open right-side up triangles), $g_2 = 2.14 \sim 2.20$ (solid spheres), and $g_4 = 2.00 \sim 2.05$ (solid upside down triangles). Figures 5(c) and (d) show the size dependencies of g_i, A_i, and ΔH_i. The values of A_4 and ΔH_4 decrease dramatically with the increase of particle size, and show a sharp drop at 42 nm. Conversely, values of A_i and ΔH_i with $i = 1, 2, 3$ do not show a significant size dependency.

4. Discussion

Recently, a complete diagonalization method and the perturbation theory method were used to calculate the axial g-tensor values (g_{II}, $g_{\perp}$) for the isolated tetrahedral $[CuO5]^{8-}$ complex of the tetrahedral YBCO [35]. Figure 6(a) shows $Cu(2)O_5$ complexes present in a tetragonal YBCO structure, where g_{II} and $g_{\perp}$ are the g-factors along the Cu(2)——O(4) and Cu(2)——O(2) bonds, respectively. The reported experimental values of $g_{II} = 2.39$ and $g_{\perp} = 2.07$ from YBCO powder samples are close to the theoretical values summarized in the first and second rows of table 2. Based on the chain-plane-paramagnetic-center model [17], the breaking of Cu(2)——O(4) bonds results in an instability of the $3d^{10}$ state of Cu(1) in the Cu(1)——O(4) chain, inducing an electron

transfer to the $3d^8$ state of Cu(2) in the CuO_2 plane, as shown in figure 6(b). The disturbance of charge equilibrium between chain and plane could result in the increase of paramagnetic complex axial g-tensors. For example, $g_{II} \sim 2.22$ and $g_{\perp} \sim 2.06$ for the orthorhombic YBCO with $\delta = 1.0$. In comparison with the overall ESR data for $Cu(2)O_5$ complexes, single crystal, and powder YBCO, the obtained g_1 and g_3 are assigned to the signal from the tetragonal YBCO phase, while g_2 and g_4 are from orthorhombic YBCO phase. It is an interesting finding that all measured NPs have coexisting tetragonal and orthorhombic phases.

However, a question remains unanswered: How does the size of YBCO NPs control the superconducting property? Since the surface defects result in broken Cu(1)——O(4) bonds, the large surface-to-volume ratio in a small NP could lead to an increase in oxygen vacancies (less oxygen content) [12], and thus T_c decreases. Figure 7(a) plots the size-dependent structure parameters, superconducting transition, and oxygen content. A significant lattice contraction along the a-axis is observed. The a decreases drastically from 3.8766 (11) Å to 3.8161(1) Å with the particle size increasing from 30 to 45 nm; meanwhile, b ($\sim$3.88 Å) does not show a significant size dependency. Contrary to single crystal and bulk YBCO, in which the lattice parameter c decreases with increasing oxygen content, c increases from 11.5926(29) Å to 11.6809(5) Å with δ increasing from 0.35 to 0.73. This result

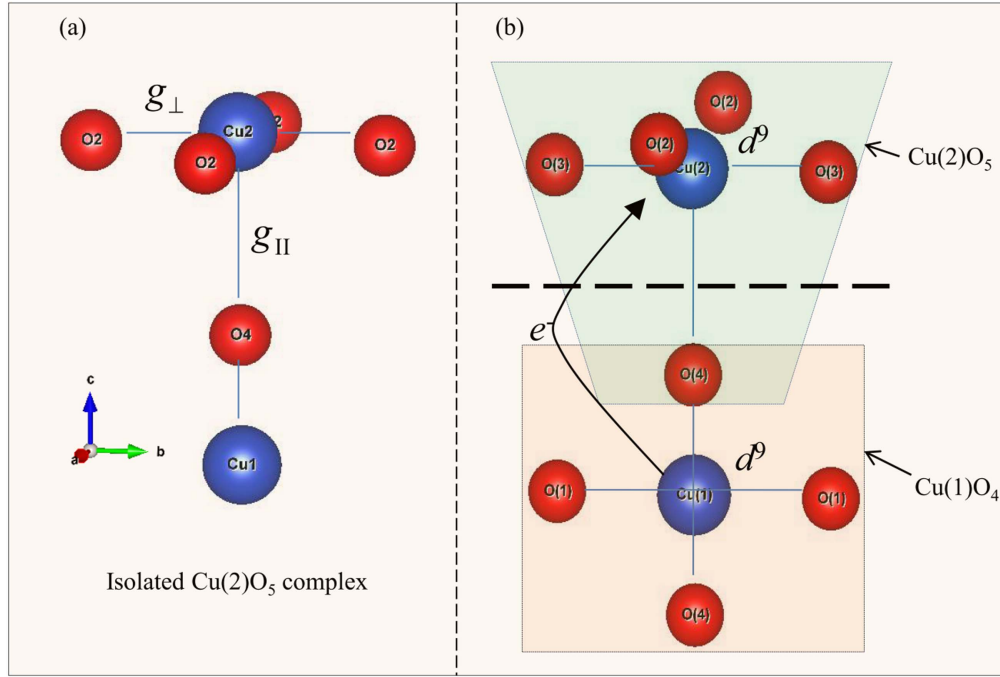**Figure 6.** A schematic diagram for (a) Cu(2)O$_5$ complexes in the tetragonal YBCO structure along the c-axis, and (b) charge transfer between the $3d^{10}$ state of Cu(1) in the chain and the $3d^8$ state of Cu(2) in the plane of the orthorhombic YBCO structure along the c-axis.

Table 2. Summary of the g-factors for YBCO NPs along with the values from the literature, including those for the isolated CuO$_5$ complex (experiment and theory), ceramic, powder samples (PD), and single crystals (SC).

Composition	$g_1(g\|\|)$	$g_3(g_\perp)$	$g_2(g\|\|)$	$g_4(g_\perp)$
Theory [35]	2.405	2.056	—	—
CuO$_5$ complex	2.409	2.054	—	—
PD, $\delta = 0.36$ (tetragonal) [17]	2.39	2.07	—	—
Ceramic (3 mm)	—	—	—	—
PD, $\delta = 1$	—	—	2.21	2.06
PD, $\delta = 1$ [36]	—	—	2.203	2.098
SC, $\delta = 0.9$ [37]	—	—	2.270	2.020
PD, $\delta = 0.95$ [38]	—	—	—	2.096(g$_{av}$)
$\delta = 0.05$	—	2.096	2.218	2.040
$\delta = 0.95$	—	2.116	2.225	2.045
$0.35 \leqslant \delta \leqslant 0.45$	—	2.121	2.229	2.048
SC, $\delta = 0.9$	—	—	2.270	2.020
This work				
NP, $\delta = 0$	2.476	2.115	2.137	2.001
NP, $\delta = 0.35$	2.483	2.111	2.201	2.016
NP, $\delta = 0.65$	2.370	2.077	2.132	2.022
NP, $\delta = 0.71$	—	2.083	2.156	2.052

Figure 7. Plot of size dependencies of (a) lattice parameters and (b) oxygen occupancy at the O(1) site; δ values (left scale) and T_C values (right scale).

suggests that the observed size dependencies of lattice parameters are mainly from the finite-size effect and less from the oxygen content. Figure 7(b) plots the δ (left) and the T_C (right) vs. $\langle d \rangle$, indicating a similar trend of T_C and δ with increasing particle size. The above results confirm that the oxygen content of the NP increases with increasing particle size, and thus T_c is enhanced.
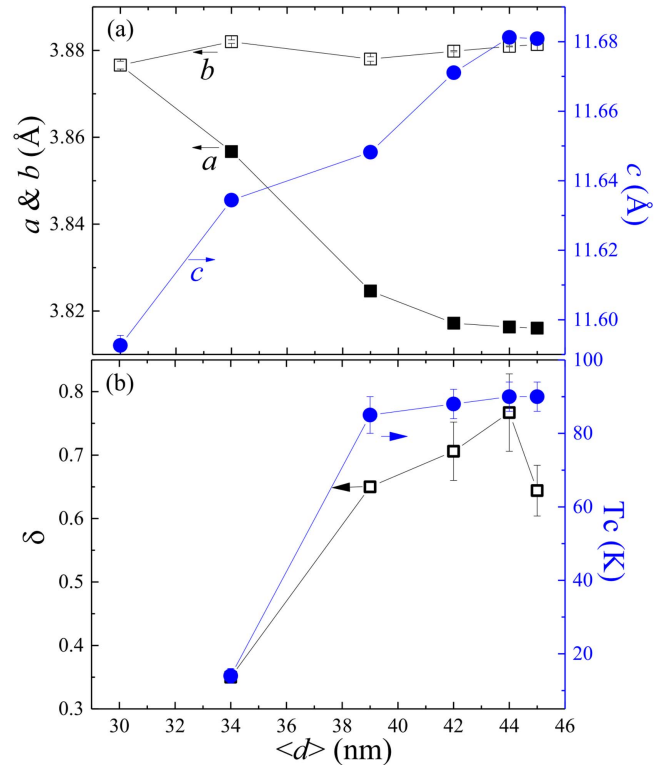
Another measure for the oxygen vacancies is the amplitude of the ESR. In general, the amount of vacancies is proportional to the amplitude of the ESR peak due to the increase of paramagnetic centers. In figure 5(c), the intensity

A_4 of the ESR peak shows a great reduction upon increasing the particle size, implying that oxygen vacancies are mainly on the CuO_2 plane. The observed reduction of ΔH_4 for the 42 nm sample suggests that the distribution of oxygen vacancies is more uniform in the large NPs. As a consequence, T_c is enhanced with increasing particle size. This study shows the advantage of utilizing the ESR technique for in-depth characterization of paramagnetic centers in oxygen-deficient complex compounds like YBCO NPs.

5. Conclusions

The crystalline and magnetic properties of microwave-assisted sol–gel-synthesized YBCO NPs (34 to 45 nm) were systematically investigated using SRXRD and ESR techniques. The finite-size effect leads to lattice contraction along the c-axis and expansion along the a-axis. A drastic rise in T_C from 14(2) K to 90(2) K is correlated with the increase in oxygen occupancy at the O(1) site in the $a-b$ plane. At room temperature, ESR spectra reveal four peaks with effective g-factors of $g_1 = 2.48 \sim 2.37$, $g_2 = 2.14 \sim 2.20$, $g_3 = 2.12 \sim 2.08$, and $g_4 = 2.00 \sim 2.05$. The (g_1, g_3) and (g_2, g_4) peaks are assigned to the axial g-tensor ($g_{\parallel}$, $g_{\perp}$) of isolated $Cu(2)O_5$ and chain-plane-paramagnetic complex, respectively. The amplitude of the ESR peak with g = 2.05 significantly decreases with increasing particle size, reflecting a reduction of oxygen vacancies in the CuO_2 plane. Our finding shows a correlation between particle size and oxygen vacancies within the finite sizes.

Notes
The authors declare no competing financial interest.

ORCID iDs

Ashish Chhaganlal Gandhi ⓘ https://orcid.org/0000-0002-1900-8702

References

[1] Wu M K, Ashburn J R, Torng C J, Hor P H, Meng R L, Gao L, Huang Z J, Wang Y Q and Chu C W 1987 Superconductivity at 93 K in a new mixed-phase Y-Ba-Cu-O compound system at ambient pressure *Phys. Rev. Lett.* **58** 908–10

[2] Jorgensen J D, Veal B W, Paulikas A P, Nowicki L J, Crabtree G W, Claus H and Kwok W K 1990 Structural properties of oxygen-deficient YBa$_2$Cu$_3$O$_{7-d}$ *Phys. Rev.* B **41** 1863–77

[3] Blinov E, Fleisher V G, Huhtinen H, Laiho R, Lähderanta E, Paturi P, Yu P S and Vlasenko L 1997 Preparation of one to three unit cell thick YBa$_2$Cu$_3$O$_{7-x}$ powders and investigation of their magnetic and microwave properties *Supercond. Sci. Technol.* **10** 818

[4] Khene S, Gasmi M and Fillion G 2015 Phase transition in YBa$_2$Cu$_3$O$_{7-\delta}$ and YBa$_2$Cu$_3$O$_{7-\delta}$/Y$_3$Fe$_5$O$_{12}$ nanoparticles at low temperatures and high fields *J. Magn. Magn. Mater.* **373** 188–94

[5] Gasmi M, Khene S and Fillion G 2013 Coexistence of superconductivity and ferromagnetism in nanosized YBCO powders *J. Phys. Chem. Solids* **74** 1414–8

[6] Khene S, Gasmi M and Fillion G 2011 Detailed elaboration method and magnetic study of nanometrical YBCO/YIG system *J. Supercond. Nov. Magn.* **24** 427–35

[7] Fan W, Zou L-J and Zeng Z 2013 Ferromagnetism on surface of YBa$_2$Cu$_3$O$_7$ particle *Physica C* **492** 80–9

[8] Arabi H, Jamshidi S, Komeili M and Amirabadizadeh A 2013 Coexistence of superconductivity and ferromagnetic phases in YBa2Cu3O7$-\delta$ nanoparticles *J. Supercond. Nov. Magn.* **26** 2069–71

[9] Zhu Z, Gao D, Dong C, Yang G, Zhang J, Zhang J, Shi Z, Gao H, Luo H and Xue D 2012 Coexistence of ferromagnetism and superconductivity in YBCO nanoparticles *Phys. Chem. Chem. Phys.* **14** 3859–63

[10] Hasanain S K, Akhtar N and Mumtaz A 2011 Particle size dependence of the superconductivity and ferromagnetism in YBCO nanoparticles *J. Nanopart. Res.* **13** 1953–60

[11] Topal U 2010 Unexpected transport and magnetic properties in Y–Ba–Cu–O superconductors *Phys. Status Solidi* A **207** 1196–203

[12] Shipra A, Gomathi A, Sundaresan A and Rao C N R 2007 Room-temperature ferromagnetism in nanoparticles of superconducting materials *Solid State Commun.* **142** 685–8

[13] Shen Z, Hu Y, Fei L, Li K, Chen W, Gu H and Wang Y 2015 Photocatalytically active YBa$_2$Cu$_3$O$_{7-x}$ nanoparticles synthesized via a soft chemical route *J. Nanomater.* **2015** 5

[14] Gazquez J *et al* 2016 Emerging diluted ferromagnetism in high-Tc superconductors driven by point defect clusters *Adv. Sci.* **3** 2198–3844

[15] de Mesquita R N *et al* 1989 ESR experiments and spectra simulations in YSa$_2$Cu$_3$O$_7$, Y$_2$SaCu$_{05}$, and SaCuO$_{2+x}$ *Phys. Rev.* B **39** 6694–9

[16] Deville A, Gaillard B, Noël H, Potel M, Gougeon P and Levet J C 1989 ESR of YBa2Cu3O7 single crystals : on the nature of the magnetic centres *J. Phys. France* **50** 2357–74

[17] Stankowski J, Hilczer W, Baszyński J, Czyżak B and Szczepańska L 1991 EPR of complex paramagnetic center in YBa$_2$Cu$_3$O$_{7-\gamma}$ induced and suppressed by mechanical processing *Solid State Commun.* **77** 125–8

[18] Tipcompor N, Thongtem T, Phuruangrat A and Thongtem S 2012 Characterization of SrCO3 and BaCO3 nanoparticles synthesized by cyclic microwave radiation *Mater. Lett.* **87** 153–6

[19] Baghurst D R, Chippindale A M and Mingos D M P 1988 Microwave syntheses for superconducting ceramics *Nature* **332** 311–311

[20] Feldstein H, Ben-Dor L and Beilin V 1994 Microwave synthesis of high Tc superconductors *Physica C* **235** 929–30

[21] Naitoh K, Takizawa T and Matsuse T 1999 Controlled Microwave Irradiation for the Synthesis of YBa 2 Cu 3 O 7 $-x$ Superconductors *Jpn. J. Appl. Phys.* **38** L724

[22] Pathak L C, Mishra S K, Bhattacharya D and Chopra K L 2004 Synthesis and sintering characteristics of Y–Ba–Cu-oxide superconductors *Mater. Sci. Eng.* B **110** 119–31

[23] Edgar A D, Nicholas G R, Pedro A Q, Mark W M and Juan C N 2015 Electrospinning of superconducting YBCO nanowires *Supercond. Sci. Technol.* **28** 015006

[24] Zhang Z, Wimbush S C, Kursumovic A, Wang H, Lee J H, Suo H and MacManus-Driscoll J L 2012 Biopolymer mediated synthesis of plate-like YBCO with enhanced grain connectivity and intragranular critical current *Cryst. Eng. Comm.* **14** 5765–70

[25] Moussa M A A, Abou-Alkheer M M, El-Hefnawy S M and Al-Nattar H I A 2009 Effect of melt processing programme on microstructure and properties of YBCO thick films *J. Supercond. Nov. Magn.* **22** 687–91

[26] Zelati A, Amirabadizadeh A and Kompany A 2011 Preparation and characterization of barium carbonate nanoparticles *Int. J. Chem. Eng. Appl.* **2** 299–303

[27] Yamamoto A, Koyama T, Mito T, Wada S, Fisher R A, Phillips N E, Wang Z P and Johnston D C 2003 Magnetic properties of copper cluster-spins in $BaCuO_{2+x}$ (x = 0 and 0.14), investigated by magnetization and nuclear magnetic resonance measurements *J. Phys. Condens. Matter* **15** 8587

[28] Boston R, Carrington A, Walsh D and Hall S R 2013 Synthesis of spherical superconductors *Cryst. Eng. Comm.* **15** 3763–6

[29] Chhaganlal G A, Hui-Yu C, Yu-Ming C and Grace L J 2016 Size confined magnetic phase in NiO nanoparticles *Mater. Res. Express* **3** 035017

[30] Rietveld H 1969 A profile refinement method for nuclear and magnetic structures *J. Appl. Crystallogr.* **2** 65–71

[31] Larson A C and Von Dreele R B 1987 General structure analysis system (GSAS) *Report* LA-UR-86-748 Los Alamos National Laboratory: Los Alamos, NM

[32] Gandhi A C, Chan T S and Wu S Y 2016 Structural phase transition in InSn nanoalloys and its impact on superconducting properties *J. Alloys Compd.* **688** 61–8

[33] Jain M and Gupta A 2007 3 Diamagnetic anisotropy of $BaCO_3$ *Diamagnetic Susceptibility and Anisotropy of Inorganic and Organometallic Compounds* ed R R Gupta (Berlin: Springer) pp 3033

[34] Wang Z R, Johnston D C, Miller L L and Vaknin D 1995 Static magnetization and ac susceptibility measurements of the copper-oxygen cluster compound $BaCuO_{2+x}$ *Phys. Rev.* B **52** 7384–94

[35] Zheng W-C, Mei Y, Yang Y-G and Su P 2012 Calculations of EPR g factors for the isolated tetragonal Cu^{2+} (II) centre in mechanically processed $YBa_2Cu_3O_{7-\delta}$ superconductors *Phys. Scripta* **86** 025702

[36] Jones R, Janes R, Armstrong R, Pyper N C, Edwards P P, Keeble D J and Harrison M R 1990 A combined ESR/X-ray diffraction study of the Y2O3-BaO-CuO phase diagram *J. Chem. Soc. Faraday Trans.* **86** 675–82

[37] Garifullin I A, Garif'yanov N N, Alekseevskii N E and Kim S F 1991 EPR data on the evolution of the oxygen distribution in single crystals of YBa2Cu3O7−δ *Physica* C **179** 9–14

[38] Shames A I, Bandyopadhyay B, Goren S D, Shaked H and Korn C 1995 *In-situ* EPR study of room-temperature evolution of YBa2Cu3O6+x ceramics *Physica* C **252** 177–82